The Astrophysical Journal Letters, 824:L6 (5pp), 2016 June 10 doi:10.3847/2041-8205/824/1/L6

BINARY NEUTRON STAR MERGERS: A JET ENGINE FOR SHORT GAMMA-RAY BURSTS

Milton Ruiz[1,2], Ryan N. Lang[1,3], Vasileios Paschalidis[4], and Stuart L. Shapiro[1,5]
[1] Department of Physics, University of Illinois at Urbana-Champaign, Urbana, IL 61801, USA
[2] Escuela de Física, Universidad Industrial de Santander, Ciudad Universitaria, Bucaramanga 680002, Colombia
[3] Leonard E. Parker Center for Gravitation, Cosmology, and Astrophysics, University of Wisconsin–Milwaukee, Milwaukee, WI 53211, USA
[4] Department of Physics, Princeton University, Princeton, NJ 08544, USA
[5] Department of Astronomy & NCSA, University of Illinois at Urbana-Champaign, Urbana, IL 61801, USA
Received 2016 April 8; revised 2016 April 22; accepted 2016 April 23; published 2016 June 3

ABSTRACT

We perform magnetohydrodynamic simulations in full general relativity (GRMHD) of quasi-circular, equal-mass, binary neutron stars that undergo merger. The initial stars are irrotational, $n = 1$ polytropes and are magnetized. We explore two types of magnetic-field geometries: one where each star is endowed with a dipole magnetic field extending from the interior into the exterior, as in a pulsar, and the other where the dipole field is initially confined to the interior. In both cases the adopted magnetic fields are initially dynamically unimportant. The merger outcome is a hypermassive neutron star that undergoes delayed collapse to a black hole (spin parameter $a/M_{\rm BH} \sim 0.74$) immersed in a magnetized accretion disk. About $4000M \sim 60(M_{\rm NS}/1.625\,M_{\odot})$ ms following merger, the region above the black hole poles becomes strongly magnetized, and a collimated, mildly relativistic outflow—an incipient jet—is launched. The lifetime of the accretion disk, which likely equals the lifetime of the jet, is $\Delta t \sim 0.1\,(M_{\rm NS}/1.625\,M_{\odot})$ s. In contrast to black hole–neutron star mergers, we find that incipient jets are launched even when the initial magnetic field is confined to the interior of the stars.

Key words: black hole physics – gamma-ray burst: general – gravitation – gravitational waves – stars: neutron

1. INTRODUCTION

The LIGO and Virgo Collaborations recently reported the first direct detection of a gravitational-wave (GW) signal and demonstrated that it was produced by the inspiral and coalescence of a binary black hole (BHBH) system (Abbott et al. 2016). This breakthrough marks the beginning of the era of GW astrophysics. GW signals are expected to be generated not only by BHBH binaries, but also by neutron star–neutron star (NSNS) and black hole–neutron star (BHNS) binaries.

Merging NSNSs and BHNSs are not only important sources of GWs, but also the two most popular candidate progenitors of *short* gamma-ray bursts (sGRBs) (Eichler et al. 1989; Narayan et al. 1992; Mochkovitch et al. 1993; Berger 2014). NSNSs and BHNSs may also generate other detectable, transient electromagnetic (EM) signals prior to (Hansen & Lyutikov 2001; McWilliams & Levin 2011; Palenzuela et al. 2013; Paschalidis et al. 2013; Ponce et al. 2014) and following (Metzger & Berger 2012; Berger 2014; Metzger et al. 2015) merger. Combining GW and EM signals from these mergers could test relativistic gravity and constrain the NS equation of state (EOS). Moreover, an association of a GW event with an sGRB (the holy grail of "multimessenger astronomy") would provide convincing evidence for the compact binary coalescence model. However, the interpretation of EM and GW signals from such mergers will rely on a theoretical understanding of these events, which requires simulations in full general relativity to treat the strong dynamical fields and high velocities arising in these scenarios. There have been multiple studies of compact binary mergers. For NSNSs, see Faber & Rasio (2012) for a review and Paschalidis et al. (2012), Gold et al. (2012), East & Pretorius (2012), Neilsen et al. (2014), Dionysopoulou et al. (2015), Sekiguchi et al. (2015), Dietrich et al. (2015), and Palenzuela et al. (2015b) for recent results. These earlier studies have advanced our knowledge of EOS effects, neutrino transport, ejecta properties, and magnetospheric phenomena. However, few studies focused on the potential for NSNSs to power sGRBs.

Recent work by Paschalidis et al. (2015b; hereafter PRS) demonstrated that mergers of magnetized BHNS systems can launch jets and be the engines that power sGRBs. The key ingredient for generating a jet was found to be the initial endowment of the NS with a dipole B-field that extends into the NS exterior as in a pulsar magnetosphere. By contrast, if the initial magnetic field is confined to the interior of the NS, no jet is observed (Etienne et al. 2012b; Kiuchi et al. 2015).

The primary motivation for this paper is to answer the question: can NSNS mergers produce jets in the same way as BHNS systems, or does this mechanism require an initial BH? Recently, it was shown that neutrino annihilation may not be strong enough to power jets (Just et al. 2016), so MHD processes must play a major role for jet formation. Previous ideal GRMHD simulations by Rezzolla et al. (2011) suggest that NSNS mergers may launch a relativistic jet, while those by Kiuchi et al. (2014), which focus on different initial configurations, show otherwise. Both of these studies have considered only scenarios where the B-field is initially confined to the *interior* of the two NSs.

Here, we describe the results of ideal GRMHD simulations of NSNSs in which we follow PRS and allow an initially strong, but dynamically unimportant dipole B-field to extend from the interior of the NSs into the exterior. We call this configuration the pulsar model (hereafter P). The existence of pulsars suggests that this may be the astrophysically most common case. As in PRS, we define an *incipient jet* as a collimated, mildly relativistic outflow which is at least partially magnetically dominated ($b^2/(2\rho_0) > 1$, where $b^2 = B^2/4\,\pi$ and ρ_0 is the rest-mass density). We find that the P configuration launches an incipient jet. To study the impact of the initial B-field geometry and to compare it with previous studies, we also perform simulations where the field is confined to the interior of the NSs (hereafter the I model), keeping its strength at the

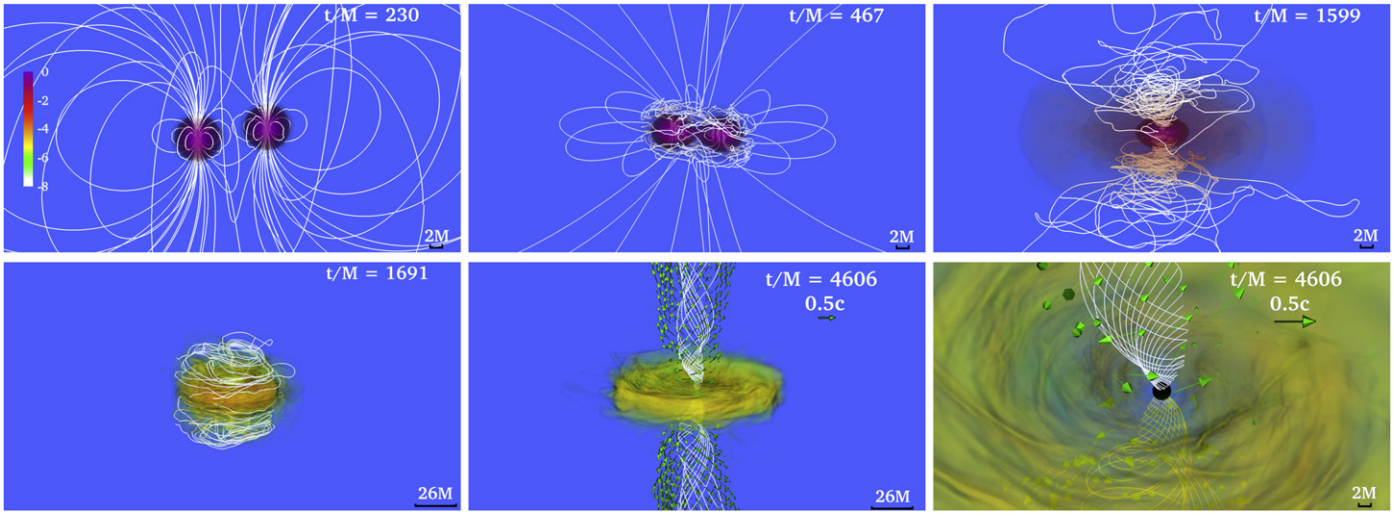

Figure 1. Snapshots of the rest-mass density, normalized to its initial maximum value $\rho_{0,\max} = 5.9 \times 10^{14}\,(1.625\,M_\odot/M_{\rm NS})^2$ g cm^{-3} (log scale) at selected times for the P case. The arrows indicate plasma velocities, and the white lines show the B-field structure. The bottom middle and right panels highlight the system after an incipient jet is launched. Here $M = 1.47 \times 10^{-2}(M_{\rm NS}/1.625\,M_\odot)$ ms $= 4.43\,(M_{\rm NS}/1.625\,M_\odot)$ km.

stellar center the same as in the P case. In contrast to BHNS systems, we find that interior-only initial B-fields also lead to jet formation in NSNSs. Throughout this work, geometrized units ($G = c = 1$) are adopted unless otherwise specified.

2. METHODS

We use the Illinois GRMHD code, which is built on the `Cactus`[6] infrastructure and uses the `Carpet`[7] code for adaptive mesh refinement. We use the `AHFinderDirect` thorn (Thornburg 2004) to locate apparent horizons. This code has been thoroughly tested and used in the past in different scenarios involving magnetized compact binaries (see, e.g., Etienne et al. 2008, 2012b; Liu et al. 2008; Gold et al. 2014a, 2014b). For implementation details, see Etienne et al. (2010, 2012a) and Farris et al. (2012).

In all simulations we use seven levels of refinement with two sets of nested refinement boxes (one for each NS) differing in size and resolution by factors of two. The finest box around each NS has a half-side length of $\sim 1.3\,R_{\rm NS}$, where $R_{\rm NS}$ is the initial NS radius. For the I model, we run simulations at two different resolutions: a "normal" resolution (model IN), in which the finest refinement level has grid spacing $0.05\,M = 227(M_{\rm NS}/1.625\,M_\odot)$ m, and a "high" resolution (model IH), in which the finest level has spacing $0.03\,M = 152(M_{\rm NS}/1.625\,M_\odot)$ m. For the P model, we always use the high resolution. These choices resolve the initial NS equatorial diameter by $\sim$120 and $\sim$180 points, respectively. In terms of grid points per NS diameter, our high resolution is close to the medium resolution used in Kiuchi et al. (2014), which covered the initial stellar diameters by $\sim$205 points. We set the outer boundary at $245M \approx 1088\,(M_{\rm NS}/1.625M_\odot)$ km and impose reflection symmetry across the orbital plane.

The quasi-equilibrium NSNS initial data were generated with the `LORENE` libraries.[8] Specifically, we use the $n = 1$, irrotational case listed in Taniguchi & Gourgoulhon (2002), Table III, $M/R = 0.14$ versus 0.14, row 3, for which the rest mass of each NS is $1.625\,M_\odot\,(k/269.6\ {\rm km}^2)^{1/2}$, with k the polytropic constant. This same case was used in Rezzolla et al. (2011). As in PRS we evolve the initial data up to the final two orbits prior to merger ($t = t_B$), at which point each NS is seeded with a dynamically unimportant B-field following one of two prescriptions:

(1) The P case (Figure 1, upper left), for which we use a dipole B-field corresponding to Equation (2) in Paschalidis et al. (2013). We choose the parameters I_0 and r_0 such that the magnetic-to-gas-pressure ratio at the stellar center is $\beta^{-1} = 0.003125$. The resulting B-field strength at the NS pole measured by a normal observer is $B_{\rm pole} \simeq 1.75 \times 10^{15}(1.625\,M_\odot/M_{\rm NS})$ G. While this B-field is astrophysically large, we choose it so that following merger, the rms value of the field strength in the hypermassive neutron star (HMNS) remnant is close to the values found in recent very-high-resolution simulations (Kiuchi et al. 2015) which showed that the Kelvin–Helmholtz instability (KHI) during merger can boost the rms B-field to $10^{15.5}$ G with local values reaching even 10^{17} G. Our choice of the B-field strength thus provides an "existence proof" for jet launching following NSNS mergers with the finite computational resources at our disposal. To capture the evolution of the exterior B-field in this case and simultaneously mimic force-free conditions that likely characterize the exterior, we follow PRS and set a variable-density atmosphere at $t = t_B$ such that the exterior plasma parameter $\beta_{\rm ext} = 0.01$. This variable-density prescription, imposed at $t = t_B$ *only*, is expected to have no impact on the outcome (cf. PRS). With our choice of $\beta_{\rm ext}$, the amount of total rest mass does not increase by more than $\sim$0.5%.

(2) The I case, which also uses a dipole field but confines it to the interior. We generate the vector potential through Equations (11), (12) in Etienne et al. (2012a), choosing $P_{\rm cut}$ to be 1% of the maximum pressure, $n_b = 2$, and A_b such that the strength of the B-field at the stellar center coincides with that in the P case. Unlike the P case, a variable-density atmosphere is not necessary, so we use a standard constant-density atmosphere with rest-mass density $10^{-10}\rho_{0,\max}$, where $\rho_{0,\max}$ is the initial maximum value of the rest-mass density.

In both the P and I cases, the magnetic dipole moments are aligned with the orbital angular momentum. During the

[6] http://www.cactuscode.org
[7] http://www.carpetcode.org
[8] http://www.lorene.obspm.fr

Table 1
Summary of Results

Case	Γ_L[a]	B_{rms}[b]	$\dot{M}$[c]	M_{disk}/M_0[d]	τ_{disk}[e]	L_{EM}[f]
P	1.25	$10^{16.0}$	0.33	1.0%	0.10	$10^{51.3}$
IN	1.21	$10^{15.8}$	0.54	1.1%	0.07	$10^{50.9}$
IH	1.15	$10^{15.7}$	0.77	1.5%	0.06	$10^{50.7}$

Notes.
[a] Maximum fluid Lorentz factor near the end of the simulation.
[b] rms value of the HMNS B-field before collapse.
[c] Rest-mass accretion rate in units of $M_\odot$ s^{-1} at $t - t_{BH} = 2100M \approx 31(M_{NS}/1.625\,M_\odot)$ ms.
[d] Ratio of disk rest mass to initial total rest mass at $t - t_{BH} = 2100M \approx 31(M_{NS}/1.625\,M_\odot)$ ms.
[e] Disk lifetime $M_{disk}/\dot{M}$ in $(M_{NS}/1.625\,M_\odot)$ s.
[f] Poynting luminosity in erg s^{-1}, time-averaged over the last $500M \sim 7.4(M_{NS}/1.625\,M_\odot)$ ms of the evolution after the jet is well -developed.

evolution, we impose a floor rest-mass density of $10^{-10}\rho_{0,max}$. We employ a Γ-law EOS, $P = \rho_0\epsilon$, with ϵ the specific internal energy, and allow for shocks.

3. RESULTS

The outcomes and basic dynamics for all our cases are similar, hence we show snapshots and discuss the evolution only for the P case, unless otherwise specified. All coordinate times will refer to the P case too, unless otherwise specified. We summarize key results for all cases in Table 1.

All cases evolve the same until merger. The two NSs orbit each other with their B-fields frozen in. Gravitational-radiation loss causes the orbit to shrink and the NSs make contact at $t = t_{merger} \approx 465M \sim 3.5(M_{NS}/1.625\,M_\odot)$ ms when the stars are oblate due to tidal effects (Figure 1, upper middle). Then a double-core remnant forms with the two dense cores rotating about each other and gradually coalescing (Figure 1, upper right).

Just before the HMNS collapses, the rms B-field strength is $\sim 10^{15.7}$–10^{16} G (see Table 1), a little larger than the values Kiuchi et al. (2015) reported, but consistent with Zrake & MacFadyen (2013).

During the HMNS stage from $t - t_{merger} \approx 115M \sim 1.7(M_{NS}/1.625\,M_\odot)$ ms up until BH formation, there is no significant enhancement of the B-field. This result is anticipated because we chose our initial B-fields such that they are near saturation ($\beta \sim$ 100–1000) following merger. We find that inside the HMNS we resolve the wavelength λ_{MRI} of the fastest-growing magneto-rotational-instability (MRI) mode by more than 10 points. In addition, λ_{MRI} fits within the HMNS, so we conclude that MRI-induced turbulence is operating during this stage. As the total rest mass of the HMNS exceeds the maximum value allowed by uniform rotation, i.e., $\sim 2.4\,M_\odot (k/269.6\,\mathrm{km}^2)^{1/2}$ for $\Gamma = 2$ (Lyford et al. 2003), it undergoes delayed collapse to a BH (Baumgarte et al. 2000; Duez et al. 2006) at $t - t_{merger} \approx 1215M \sim 18(M_{NS}/1.625\,M_\odot)$ ms in both the P and IN cases. In the IH case, collapse takes place later at $t - t_{merger} \approx 2135M \sim 31.5(M_{NS}/1.625\,M_\odot)$ ms. The sensitivity of the collapse time for short-lived HMNSs to the B-field is physical and has been observed previously (Giacomazzo et al. 2011). Its dependence on resolution, even in purely hydrodynamic simulations, has been noted as well (Paschalidis et al. 2015a; East et al. 2016).

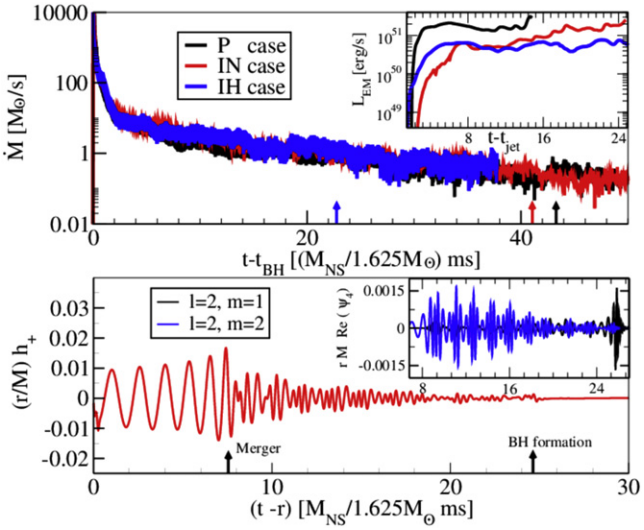

Figure 2. Top: rest-mass accretion rate $\dot{M}$. The arrows indicate the time (t_{jet}) at which the incipient jet reaches $z = 100\,M$. The inset shows the outgoing EM luminosity for $t > t_{jet}$ computed on a coordinate sphere of radius $r = 115M \approx 510(M_{NS}/1.625\,M_\odot)$ km. Bottom: GW amplitude h_+ vs. retarded time for the P case. The inset focuses on the post-merger phase, showing the $(l, m) = (2, 2)$ and $(l, m) = (2, 1)$ (multiplied by 20) modes of the Newman–Penrose scalar Ψ_4.

In all cases the BH has a mass of $M_{BH} \approx 2.85\,M_\odot(M_{NS}/1.625\,M_\odot)$ with spin $a/M \simeq 0.74$ at high resolution, or $a/M \simeq 0.8$ at normal resolution.

Shortly after BH formation, plasma velocities above the BH poles point toward the BH (apart from some material ejected during merger), but the winding of the B-field above the BH poles is well underway (Figure 1, bottom left). By $t - t_{BH} \approx 2800\,M \sim 41(M_{NS}/1.625\,M_\odot)$ ms, where t_{BH} is the BH formation time, the B-field has been wound into a helical funnel (Figure 1, bottom middle and right). Unlike in the BHNS case of PRS, the B-field does not grow following BH formation: the existence of the HMNS phase instead allows the B-field to build to saturation levels prior to BH formation. We do observe a gradual growth in $b^2/(2\rho_0)$ above the BH pole from $\sim$1 to $\sim$100, due to the emptying of the funnel as matter accretes onto the BH. At $t - t_{BH} \approx 2000M \sim 30(M_{NS}/1.625\,M_\odot)$ ms, the fluid velocities begin to turn around and point outward. At $t - t_{BH} \approx 2900M \sim 43(M_{NS}/1.625\,M_\odot)$ ms, the outflow extends to heights greater than $100M \sim 445(M_{NS}/1.625\,M_\odot)$ km. At this point an incipient jet has formed (Figure 1, bottom middle and right). We observe similar evolution in the I cases, although in the IH case the incipient jet is well-developed by $t - t_{BH} \sim 1550M \sim 23(M_{NS}/1.625\,M_\odot)$ ms, while in the IN case it takes $t - t_{BH} \sim 2850\,M \sim 42(M_{NS}/1.625\,M_\odot)$ ms for the incipient jet to be launched (see the arrows in Figure 2).

In all cases, the accretion rate $\dot{M}$ begins to settle into a steady state at $t - t_{BH} \approx 1350M \sim 20(M_{NS}/1.625M_\odot)$ ms and slowly decays thereafter (Figure 2, top). At $t - t_{BH} \approx 2100M \sim 31(M_{NS}/1.625M_\odot)$ ms, the accretion rate is roughly $0.33\,M_\odot$ s^{-1}, at which time the disk mass is $\sim 0.05\,M_\odot(M_{NS}/1.625M_\odot)$. Thus, the disk will be accreted in $\Delta t \sim M_{disk}/\dot{M} \sim 0.1$ s, implying that the engine's fuel will be exhausted on a timescale consistent with the duration of the very short-duration sGRBs (see, e.g., Kann et al. 2011).

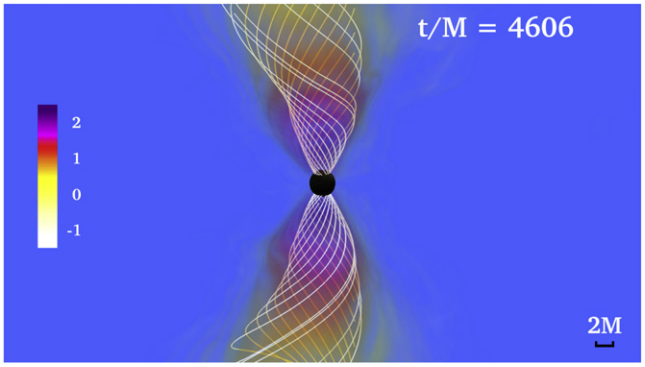

Figure 3. Ratio $b^2/(2\rho_0)$ (log scale) at $t - t_{\rm merger} \approx 4135M \sim 61(M_{\rm NS}/1.625\,M_\odot)$ ms for the P case. The white lines indicate the B-field lines plotted in the funnel where $b^2/(2\rho_0) \geqslant 10^{-2}$. Magnetically dominated areas ($b^2/(2\rho_0) \geqslant 1$) extend to heights greater than $20M \approx 20\,r_{\rm BH}$ above the BH horizon (the black sphere). Here $r_{\rm BH} = 2.2(M_{\rm NS}/1.625\,M_\odot)$ km.

In the BH–accretion disk system, we again resolve $\lambda_{\rm MRI}$ by more than 10 grid points. For the most part, $\lambda_{\rm MRI}$ fits inside the disk. MRI is thus operating in these simulations, but it is saturated, with the toroidal and poloidal B-field components approximately equal in magnitude and not growing. Near the end of the simulations the B-field magnitude above the BH pole is $\sim 10^{16}$ G.

As in PRS, we have tracked the motion of individual Lagrangian fluid tracers. We find that they follow the expected helical motion of the outflow and that the gas pouring into the funnel and comprising the outflow originates from the disk. This test confirms the physical nature of the jet.

During the inspiral and throughout BH formation, GWs are emitted with the $(l, m) = (2, 2)$ mode being dominant. This includes quasi-periodic spindown GWs from the transient HMNS (Shibata 2005; for a review and references, see Baumgarte & Shapiro 2010). However, we find that $(l, m) = (2, 1)$ GW modes also develop during and after merger (Figure 2, bottom). While we see no evidence for a one-arm instability (Paschalidis et al. 2015a), $m = 1$ modes may be generated from asymmetries in the two cores following merger. Like post-merger $m = 2$ modes, $m = 1$ modes due to asymmetries in the two cores of double-core HMNSs may be used to constrain the NS EOS.

Figure 3 displays the ratio $b^2/(2\rho_0)$ at $t - t_{\rm merger} \approx 4200M \sim 68(M_{\rm NS}/1.625\,M_\odot)$ ms. Magnetically dominated areas ($b^2/(2\rho_0) > 1$) extend to heights $\gtrsim 20M \approx 20\,r_{\rm BH}$ above the BH, where $r_{\rm BH}$ is the BH apparent horizon radius. Using the $b^2/(2\rho_0) \sim 10^{-2}$ contour as a rough definition for the funnel boundary, the funnel opening half-angle is $\sim 20°$–$30°$, which is consistent with PRS. The maximum value of the Lorentz factor inside the funnel is $\Gamma_{\rm L} \sim 1.1$–1.25 (see Table 1), implying only a mildly relativistic flow. However, steady-state and axisymmetric jet models (Vlahakis & Königl 2003) show that the maximum attainable value of $\Gamma_{\rm L}$ is approximately equal to $b^2/(2\rho_0)$, which reaches values $\gtrsim 100$ within the funnel. Hence, these incipient jets may be accelerated to $\Gamma_{\rm L} \sim 100$, as is necessary to explain sGRB phenomenology. (However, our code may not be reliable at values of $b^2/(2\rho_0) > 100$.) In the asymptotically flat region at heights greater than $100M \sim 650(M_{\rm NS}/1.625\,M_\odot)$ km, the specific energy $E = -u_0 - 1 > 0$ is always positive and therefore the outflowing plasma is unbound.

To assess if the Blandford–Znajek (BZ) effect (Blandford & Znajek 1977) is operating in our system as in PRS, we measure the ratio of the angular frequency of the B-field, Ω_F, to the angular frequency of the BH, Ω_H. On an $x - z$ meridional slice passing through the BH centroid and along coordinate semicircles of radii $r_{\rm BH}$ and $2r_{\rm BH}$, we find that $\Omega_F/\Omega_H \sim 0.1$–$0.25$ within an opening angle of 20° from the BH rotation axis, within which the force-free BZ solution might apply. The observed deviation of Ω_F/Ω_H from the split-monopole value ~0.5 can be due either to the gauge in which we compute Ω_F, deviations from a split-monopole B-field, or possibly from inadequate resolution. The outgoing Poynting luminosity is $L_{\rm EM} \sim 10^{50.7}$–$10^{51.3}$ erg s^{-1} (see Figure 2, Table 1), which is only a little less than the EM power expected from the BZ effect (Thorne et al. 1986): $L_{\rm EM} \sim 10^{52}\,[(a/M_{\rm BH})/0.75]^2\,(M_{\rm BH}/2.8\,M_\odot)^2\,(B/10^{16}\,{\rm G})^2$ erg s^{-1}. The BZ effect is likely operating here, but higher resolution may be necessary to match the expected luminosity more closely.

4. CONCLUSIONS

We showed that an NSNS system with an initially high but dynamically weak B-field launches an incipient jet (an unbound, collimated, and mildly relativistic outflow). This occurs following the delayed collapse of the HMNS, both for initially dipole B-fields which extend from the NS interior into its exterior and initially dipole B-fields confined to the interior. This last result differentiates NSNSs from BHNSs. The accretion timescale of the remnant disk and energy output are consistent with very short sGRBs, demonstrating that NSNSs can indeed provide the central engines that power such phenomena. Our results were obtained with high initial B-fields, which match the post-merger expectations from B-field amplification due to the KHI. However, to capture the KHI-induced B-field growth, resolutions about five times higher than those adopted here are necessary. Evolving for $4000M \sim 60(M_{\rm NS}/1.625\,M_\odot)$ ms at such high resolution would take years with current resources. The simulations presented here show that if the B-fields in NSNS mergers can be amplified by the KHI to $\gtrsim 10^{15.5}$ G, then these systems are viable sGRB engines. We anticipate, but have not yet proved, that jets can be launched even if one starts with B-field strengths of order 10^{12} G. We also expect that the time interval between merger and jet launch will be longer the weaker the initial B-field.

Different EOSs affect details such as the amount of disk mass, as well as the ejection of different amounts of matter (see e.g., Hotokezaka et al. 2013; Palenzuela et al. 2015a), and therefore the ram pressure of the atmosphere surrounding the remnant BH-disk system. The above may be the main reason for the non-observance of an incipient jet in the NSNS simulations reported by Kiuchi et al. (2014). We infer from their description that the merger with their adopted EOS ejects more matter in the atmosphere with longer fall-back time than in our cases. For the outflow to emerge, the B-field must overcome the ram pressure of the infalling matter. The only way for this to happen is if the ambient matter density decreases with time, which occurs because the atmosphere becomes thinner as it accretes onto the BH. Kiuchi et al. (2014) reported that at $t - t_{\rm BH} \sim 26$ ms, there still is matter in the atmosphere that is accreting, hence the ram pressure is larger

than the *B*-field pressure. It is likely that their calculations require longer integration times for an incipient jet to emerge.

Recently, NSNS simulations with a weaker interior-only initial *B*-field were carried out by Endrizzi et al. (2016). Their resolution was too low to capture MRI or the KHI, hence the *B*-field did not amplify appreciably and as a result, no jets were observed.

A few caveats remain. First, several quantities are sensitive to resolution, such as the HMNS lifetime and the exact EM Poynting luminosity. However, other evolution characteristics, such as HMNS formation following NSNS merger, delayed collapse, the remnant BH mass and spin, the disk mass, and the ultimate emergence of the incipient jet are almost insensitive to resolution. The above conclusions suggest that higher resolutions than those adopted here are necessary for very accurate calculations, but the essential nature of incipient jet emergence is robust. Second, there is microphysics that we do not model here, such as the effects of a realistic hot, nuclear EOS and neutrino transport. We plan to implement such processes and address all of the aforementioned issues in future studies.

We thank the Illinois Relativity Group REU team members Sean E. Connelly, Cunwei Fan, Abid Khan, and Patchara Wongsutthikoson for their assistance in creating Figures 1 and 3. This work has been supported in part by NSF grant PHY-1300903 and NASA grant NNX13AH44G at the University of Illinois at Urbana-Champaign. M.R. was also supported in part by Colciencias under program "Es tiempo de Volver." R.L. acknowledges support from a Fortner Fellowship at UIUC as well as NSF grant PHY-1307429. V.P. acknowledges support from the Simons foundation and NSF grant PHY-1305682. This work made use of the Extreme Science and Engineering Discovery Environment (XSEDE), which is supported by National Science Foundation grant number ACI-1053575. This research is part of the Blue Waters sustained-petascale computing project, which is supported by the National Science Foundation (awards OCI-0725070 and ACI-1238993) and the state of Illinois. Blue Waters is a joint effort of the University of Illinois at Urbana-Champaign and its National Center for Supercomputing Applications.

REFERENCES

Abbott, B. P., Abbott, R., Abbott, T. D., et al. 2016, PhRvL, 116, 061102
Baumgarte, T. W., & Shapiro, S. L. 2010, Numerical Relativity: Solving Einstein's Equations on the Computer (Cambridge: Cambridge Univ. Press)
Baumgarte, T. W., Shapiro, S. L., & Shibata, M. 2000, ApJL, 528, L29
Berger, E. 2014, ARA&A, 52, 43
Blandford, R. D., & Znajek, R. L. 1977, MNRAS, 179, 433
Dietrich, T., Bernuzzi, S., Ujevic, M., & Bruegmann, B. 2015, PhRvD, 91, 124041
Dionysopoulou, K., Alic, D., & Rezzolla, L. 2015, PhRvD, 92, 084064
Duez, M. D., Liu, Y. T., Shapiro, S. L., Shibata, M., & Stephens, B. C. 2006, PhRvL, 96, 031101
East, W. E., Paschalidis, V., Pretorius, F., & Shapiro, S. L. 2016, PhRvD, 93, 024011
East, W. E., & Pretorius, F. 2012, ApJL, 760, L4
Eichler, D., Livio, M., Piran, T., & Schramm, D. N. 1989, Natur, 340, 126
Endrizzi, A., Ciolfi, R., Giacomazzo, B., Kastaun, W., & Kawamura, T. 2016, CQGra, submitted (arXiv:1604.03445)
Etienne, Z. B., Faber, J. A., Liu, Y. T., et al. 2008, PhRvD, 77, 084002
Etienne, Z. B., Liu, Y. T., Paschalidis, V., & Shapiro, S. L. 2012a, PhRvD, 85, 064029
Etienne, Z. B., Liu, Y. T., & Shapiro, S. L. 2010, PhRvD, 82, 084031
Etienne, Z. B., Paschalidis, V., & Shapiro, S. L. 2012b, PhRvD, 86, 084026
Faber, J. A., & Rasio, F. A. 2012, LRR, 15, 8
Farris, B. D., Gold, R., Paschalidis, V., Etienne, Z. B., & Shapiro, S. L. 2012, PhRvL, 109, 221102
Giacomazzo, B., Rezzolla, L., & Baiotti, L. 2011, PhRvD, 83, 044014
Gold, R., Bernuzzi, S., Thierfelder, M., Brügmann, B., & Pretorius, F. 2012, PhRvD, 86, 121501
Gold, R., Paschalidis, V., Etienne, Z. B., Shapiro, S. L., & Pfeiffer, H. P. 2014a, PhRvD, 89, 064060
Gold, R., Paschalidis, V., Ruiz, M., et al. 2014b, PhRvD, 90, 104030
Hansen, B. M., & Lyutikov, M. 2001, MNRAS, 322, 695
Hotokezaka, K., Kiuchi, K., Kyutoku, K., et al. 2013, PhRvD, 87, 024001
Just, O., Obergaulinger, M., Janka, H.-T., Bauswein, A., & Schwarz, N. 2016, ApJL, 816, L30
Kann, D. A., Klose, S., Zhang, B., et al. 2011, ApJ, 734, 96
Kiuchi, K., Cerd-Durn, P., Kyutoku, K., Sekiguchi, Y., & Shibata, M. 2015, PhRvD, 92, 124034
Kiuchi, K., Kyutoku, K., Sekiguchi, Y., Shibata, M., & Wada, T. 2014, PhRvD, 90, 041502
Kiuchi, K., Sekiguchi, Y., Kyutoku, K., et al. 2015, PhRvD, 92, 064034
Liu, Y. T., Shapiro, S. L., Etienne, Z. B., & Taniguchi, K. 2008, PhRvD, 78, 024012
Lyford, N. D., Baumgarte, T. W., & Shapiro, S. L. 2003, ApJ, 583, 410
McWilliams, S. T., & Levin, J. 2011, ApJ, 742, 90
Metzger, B. D., Bauswein, A., Goriely, S., & Kasen, D. 2015, MNRAS, 446, 1115
Metzger, B. D., & Berger, E. 2012, ApJ, 746, 48
Mochkovitch, R., Hernanz, M., Isern, J., & Martin, X. 1993, Natur, 361, 236
Narayan, R., Paczynski, B., & Piran, T. 1992, ApJL, 395, L83
Neilsen, D., Liebling, S. L., Anderson, M., et al. 2014, PhRvD, 89, 104029
Palenzuela, C., Lehner, L., Ponce, M., et al. 2013, PhRvL, 111, 061105
Palenzuela, C., Liebling, S. L., Neilsen, D., et al. 2015a, PhRvD, 92, 044045
Palenzuela, C., Liebling, S. L., Neilsen, D., et al. 2015b, PhRvD, 92, 044045
Paschalidis, V., East, W. E., Pretorius, F., & Shapiro, S. L. 2015a, PhRvD, 92, 121502
Paschalidis, V., Etienne, Z. B., & Shapiro, S. L. 2012, PhRvD, 86, 064032
Paschalidis, V., Etienne, Z. B., & Shapiro, S. L. 2013, PhRvD, 88, 021504
Paschalidis, V., Ruiz, M., & Shapiro, S. L. 2015b, ApJL, 806, L14
Ponce, M., Palenzuela, C., Lehner, L., & Liebling, S. L. 2014, PhRvD, 90, 044007
Rezzolla, L., Giacomazzo, B., Baiotti, L., et al. 2011, ApJL, 732, L6
Sekiguchi, Y., Kiuchi, K., Kyutoku, K., & Shibata, M. 2015, PhRvD, 91, 064059
Shibata, M. 2005, PhRvL, 94, 201101
Taniguchi, K., & Gourgoulhon, E. 2002, PhRvD, 66, 104019
Thornburg, J. 2004, CQGra, 21, 743
Thorne, K. S., Price, R. H., & Macdonald, D. A. 1986, The Membrane Paradigm (New Haven, CT: Yale Univ. Press)
Vlahakis, N., & Königl, A. 2003, ApJ, 596, 1080
Zrake, J., & MacFadyen, A. I. 2013, ApJL, 769, L29